# Preparation and Characterization of Tunable Oil-Encapsulated Alginate Microfibers

A. S. Chaurasia,[a] F. Jahanzad[b] and S. Sajjadi[a†]

[a]Department of Physics, King's College London, Strand, London, WC2R 2LS, UK

[b]Division of Chemical and Petroleum Engineering, London South Bank University, London, SE1

A single-step microfluidic approach was developed which allowed a wide range of oil-loaded calcium-alginate microfibers to be fabricated at the same compositions but with different morphologies. A framework for characterization of wavy fibers was developed which linked the fiber morphology and tensile strength to the encapsulation type and geometry. The geometry of oil encapsulates as well as the fibers surface morphology were conveniently tuned via the gelation reaction dynamics and phase flow rates. A 2D mathematical reconstruction of the fiber's surface revealed that fibers having spherical and ellipsoid encapsulates enjoyed the highest surface roughness. Tubular fibers endured the highest tensile force before failure, compared to fibers with other encapsulate geometries at a fixed alginate phase ratio ($\phi_{alg}$). Fibers with increased $\phi_{alg}$ withstood a higher tensile force. However, the strength of fibers reduced if the increase in $\phi_{alg}$ altered the encapsulate geometry from tubular to discrete oil segments. Tubular fibers also underwent maximum elastic and plastic deformation prior to failure, among all fibers. *Keywords:* Microfluidics, wet spinning, compound fibers, tensile strength, sodium alginate, gelation.

## 1. Introduction

Microfibers of calcium alginate, a biocompatible hydrogel material, are widely used for several biomedical applications such as wound healing,[1,2,3] and cell encapsulation.[4] These fibers are also commonly used for making complex fibrous networks, such as 3D scaffolds used in tissue engineering.[5,6,7,8,9] Microfibers in such applications are often subjected to frequent and enduring tensile loading during their handling and usage[10] and thus require superior physical and mechanical properties.[11]

With a recent surge in technological innovations, an increasingly wide variety of novel hydrogel fibers are being reported. These compound microfibers are often tailored to possess highly structured interiors in the form of encapsulates[12] with a precisely tuned composition.[13] Such compound fibers are ideally suited for conferring multi-functionality to hydrogel microfibers.[14] For example, compound alginate microfibers have been used as micro-carriers of a range of hydrophobic encapsulates, such as multi-cellular aggregates, oil-soluble drugs[15], and magnetic oil droplets, for advanced fiber manipulation and assembly operations[16] and also for hierarchical storage and triggered release of encapsulates.[17,18] The presence of encapsulates can also alter the surface morphology of fibers and increase their surface area advantage of which has been taken in wettability related applications such as enhancing water collection ability.[19]

Given the wide range of applications, these compound microfibers are required to possess desirable physical features and mechanical properties, such as low spillage ratio and high tensile strength. However, the encapsulation of a liquid phase in a fiber reduces the fiber strength, since a part of the solid polymer is replaced by the encapsulated liquid phase. Furthermore, the fibers morphology can vary from segmented to tubular shapes with changing encapsulate geometry. Therefore, a comparative study to analyse the impact of encapsulate geometry on fiber properties is of high significance.

While there have been several studies on mechanical properties of synthetic fibers,[20] and also simple and composite hydrogel fibers,[21,22,23] reports on mechanical testing of compound hydrogel microfibers are extremely scarce in the literature. This is due to the fact that production of compound fibers by conventional techniques is restricted to either segmented hydrophobic encapsulates,[14,15,16,17] or tubular hydrophilic encapsulates.[13,15,24] In a rare report, He et al. conducted the uniaxial tensile testing of individual chitosan microfibers with segmented and tubular encapsulates, formed using different types of internal phase, and analysed the effect of shell thickness on the fiber strength. However, this lack of consistency in production of variety of encapsulate geometries can limit the comparative studies of microfibers produced by different techniques and also translate into further uncertainty due to the change of encapsulate phase.

Here we report an extensive investigation into the tensile testing of a wide range of oil-encapsulated alginate microfibers, to highlight the impact of encapsulate geometry and the alginate phase ratio ($\phi_{alg}$), in addition to the shell thickness, on the fiber properties. In this report, we employ our recently developed flexible one-step method[12,18] to fabricate oil-loaded microfibers with a whole range of encapsulate geometry, which can provide a sound platform for comparative characterization of microfibers structures. We show how fiber morphology can be tuned by controlling the rate of gelation during encapsulation. We also report a detailed framework for characterization of oil-encapsulated fibers, which shows how encapsulation geometry and surface morphology can affect the mechanical strength of the resulting fibers, which is of prime importance for biomedical applications of microfibers.

## 2. Experimental Section

### 2.1 *Materials*

Sodium alginate and calcium chloride (Sigma Aldrich) were used as received. De-ionized water was used as the middle and external phase. Octane (99%, Sigma Aldrich) was used as received as the model inner oil phase. A water-soluble dye (trypan blue) was used in the alginate phase for contrast imaging, unless mentioned otherwise.

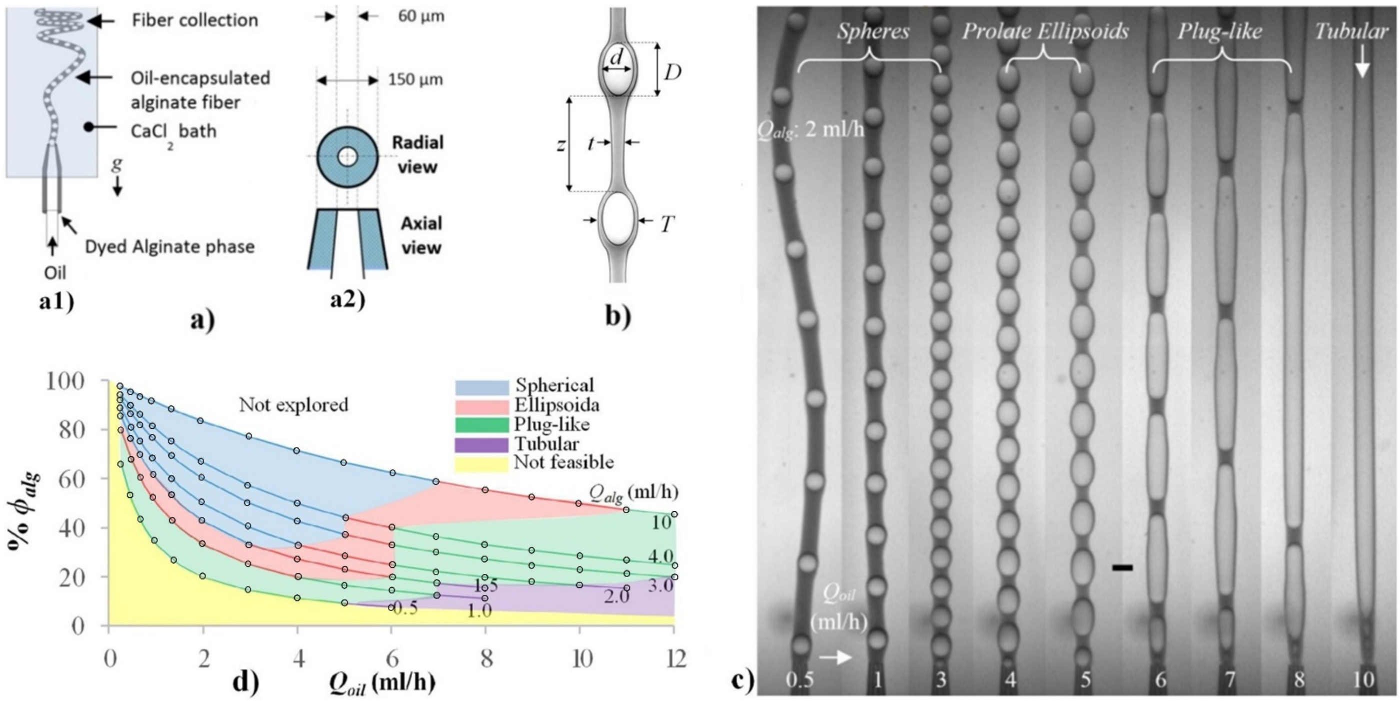

**Figure 1** **(a)** A schematic of the one-step microfluidic device, which was used to produce oil-encapsulated alginate fiber, is shown in (a1). The coaxial alignment and dimensions of the tapered glass capillary tips are presented in (a2). **(b)** An optical micrograph of a produced oil-loaded microfiber, which also shows the various nomenclatures assigned to its geometry. A water-soluble dye (trypan blue) was used in the alginate phase. **(c)** A series of micrographs shows the variations in the shape of the oil segments encapsulated within the alginate fibers with $Q_{oil}$ at a given middle alginate phase flow rate ($Q_{alg}$= 2 ml/h). The encapsulate geometry can be tuned from a segmented encapsulation (having spherical, ellipsoidal or plug-like shapes) to a continuous (tubular) encapsulation. Scale bar: 200 µm. **(d)** Percentage alginate phase ratio at different flow conditions. The *x*-axis is $Q_{oil}$, while the solid lines indicate the fixed $Q_{alg}$ conditions. The investigated flow conditions are marked by circular symbols. All data obtained by using 1 wt% alginate and 4 wt% $CaCl_2$ concentrations.

## 2.2 *Device and Procedure*

Figure 1a shows a schematic of the glass capillary microfluidic device used to achieve the single-step oil encapsulation within alginate fibers. Two glass capillaries, circular (ID: 0.56 mm, OD: 1 mm) and square (IL: 1 mm, OL: 1.5 mm), were pulled using a pipette puller (P-1000, Sutter Instrument, Novato, USA). The tapered tips were cut to the desired sizes, and the inner tip (ID: 40 µm, OD: 60 µm) was coaxially aligned with the outer tip (ID: 150 µm, OD: 175 µm) at the same level. The coaxially aligned capillary setup was introduced vertically into a wide cuvette, which housed the quiescent outer aqueous calcium chloride solution, as shown in Figure 1a1. The middle aqueous alginate phase was introduced through the interstitial spaces between the middle and inner capillaries, into the outer phase to form calcium alginate fibers. The oil phase was pumped (using a syringe pump from Harvard Apparatus) through the inner capillary, which produced oil-loaded alginate fibers, an example of which is shown in Figure 1b. The fibers were collected at the top of the cuvette, facilitated by the buoyancy force exerted by the encapsulated oil phase. This buoyancy-assisted microfluidic setup has previously been used to generate oil-loaded alginate microfibers with asymmetric oil-encapsulates, and millimetric core-shell drops with tunable shell thickness.[25,26] A high-speed video recording camera (Photron FastCam SA-5 monochrome) was used to record fiber formation.

The tensile testing of the fibers was conducted with the help of an extremely sensitive force-sensing device (DCA-100, First Ten Angstroms), which is controlled via its computer software. The device has an immobile jaw holding a metal hanger on its top section, which is coupled with a built-in force sensing mechanism. The bottom stage, which is integrated with a stepper motor, can be moved upwards or downwards in the vertical direction at a desired velocity. All the fibers were cut to a fixed length, which were mounted using a metal hanger at the top and glued at the bottom. The glue (Devcon 5-minute epoxy) was left overnight to harden completely before conducting the testing.

## 3. Results and Discussion

### *3.1 Factors affecting fiber and encapsulate morphologies*

We employed the flexible single-step microfluidic encapsulation approach recently developed by us to fabricate oil-in-alginate fibers with a tunable encapsulate geometry ranging from spherical and ellipsoidal to plug-like and tubular (Figure 1a).[18,12]

The assigned nomenclatures for fibers are shown in Figure 1b. Figure 1c shows the evolution of morphology for fibers encapsulating discrete oil segments including spheres, prolate ellipsoids (referred to as *ellipsoid* for simplicity) and plug-like to those having a single straight tube filled up with oil, all obtained via increasing the inner oil phase volumetric flow rate ($Q_{oil}$) at a constant middle alginate phase flow rate ($Q_{alg}$).

Sodium alginate and calcium ions react, as soon as they are brought into contact, and produce calcium-alginate gels. The rate of gelation, which plays a decisive role in controlling the shape of encapsulated entities and the resulting fiber morphology, depends on the concentration of calcium ions and alginate. Examples of fiber morphologies made by alteration of $CaCl_2$ and alginate concentrations are given in Figure 2a and 2b, respectively.

Figure 2a clearly shows the evolution of fiber morphology from wavy to flat with increasing $CaCl_2$ concentration. A high calcium chloride concentration resulted in the formation of a highly cross-linked (non-deformable) interface, which was able to resist the radial expansion of drops at the tip and act such as virtual tube to guide them through, and produce flat fibers with encapsulates with a radial diameter ($d$) smaller than the fiber thickness ($t$). This eliminated the need to generate the internal droplets or encapsulates upstream the tip in order to engulf them inside the fibers, thus making it possible to create straight and wavy fibers using a single set up. The alginate-water interface at high $CaCl_2$ concentration was dense, prominent and visible, evidenced by Figure 2a, as a result of faster gelation due to the abundance of $Ca^+$ ions.

A low concentration of $CaCl_2$ formed a light and nearly invisible gelled interface, marked with white dashed lines in Figure 2a for fibers using 0.1-1.0 wt% $CaCl_2$. This interface could be easily deformed by the inner oil drops, leading to the formation of wavy fibers.

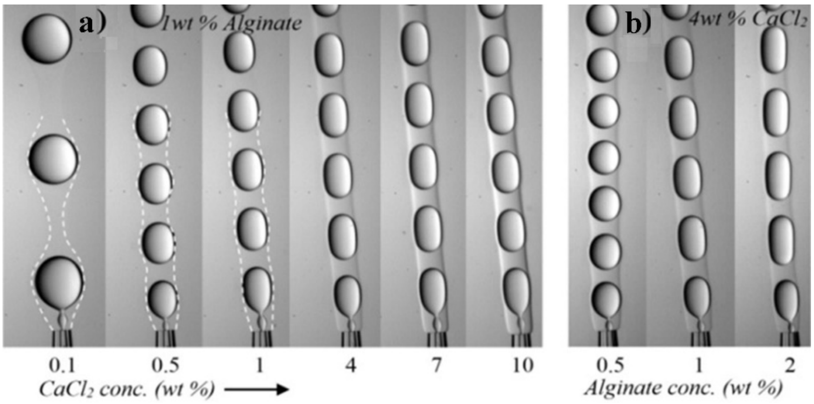

**Figure 2** Micrographs show the shape variation of the encapsulated oil segments by varying the concentration of **(a)** $CaCl_2$ and **(b)** alginate in the outer and middle phase, respectively. The flow conditions are $Q_{alg}$ = 3 ml/h and $Q_{oil}$ = 5 ml/h.

Figure 2b shows similar pattern for evolution of fiber morphology with increasing alginate concentration. We did not use alginate concentrations below 0.50 wt% because of lack of strength in the resulting fibers. Figure 2b also shows that the drops formed under the same flow rate conditions exhibit larger aspect ratio at higher alginate concentrations due to the resistance imposed by the more robust gelling interface.

The flow conditions can also affect the morphology of fibers by altering the time scale during which effective gelling occurs. A typical encapsulate formation time is as small as few milliseconds thereby allowing encapsulates to deform the alginate shell to form wavy fiber structures, before the gelation kinetics can progress significantly. Figure 1 shows how a wide range of fiber morphologies was obtained by regulating the flow rate despite using a high $Ca^{2+}$ concentration.

### 3.2 *Features of oil-loaded fibers*

A fiber is featured by its high axial-to-radial dimension ratio. Most fibers have a flat smooth surface; however, this may be altered by modifying the fabrication method[27] or by incorporating discrete entities of an immiscible phase into fibers. This latter can switch the smooth surface morphology of fibers to wavy profile, as observed in the case of oil-encapsulated fibers.[14,18] Wavy fibers can be characterized for a range of properties including *degree of waviness*, *spillage ratio*, and *tensile properties*.

### 3.2.1 Degree of waviness

The 2D surface profile of wavy oil-loaded fibers can be best represented by a sinusoidal function, as defined in Figure 3a1. The encapsulated oil entities, which are the main reason for waviness of the fibers, can be represented by an independent elliptical function for simplicity (Figure 3a2). Figure 3b illustrates the mathematical reconstruction of the surface profile of the oil-loaded fibers shown in Figure 1c ($Q_{oil}$= 0.5 ml/h - 6 ml/h). The encapsulate frequency, or the number of oil segments per unit length, is represented by $(z+D)^{-1}$, while the amplitude, or the maximum fiber thickness with respect to the minimum fiber thickness $t/2$, can be expressed by $(T-t)/2$.

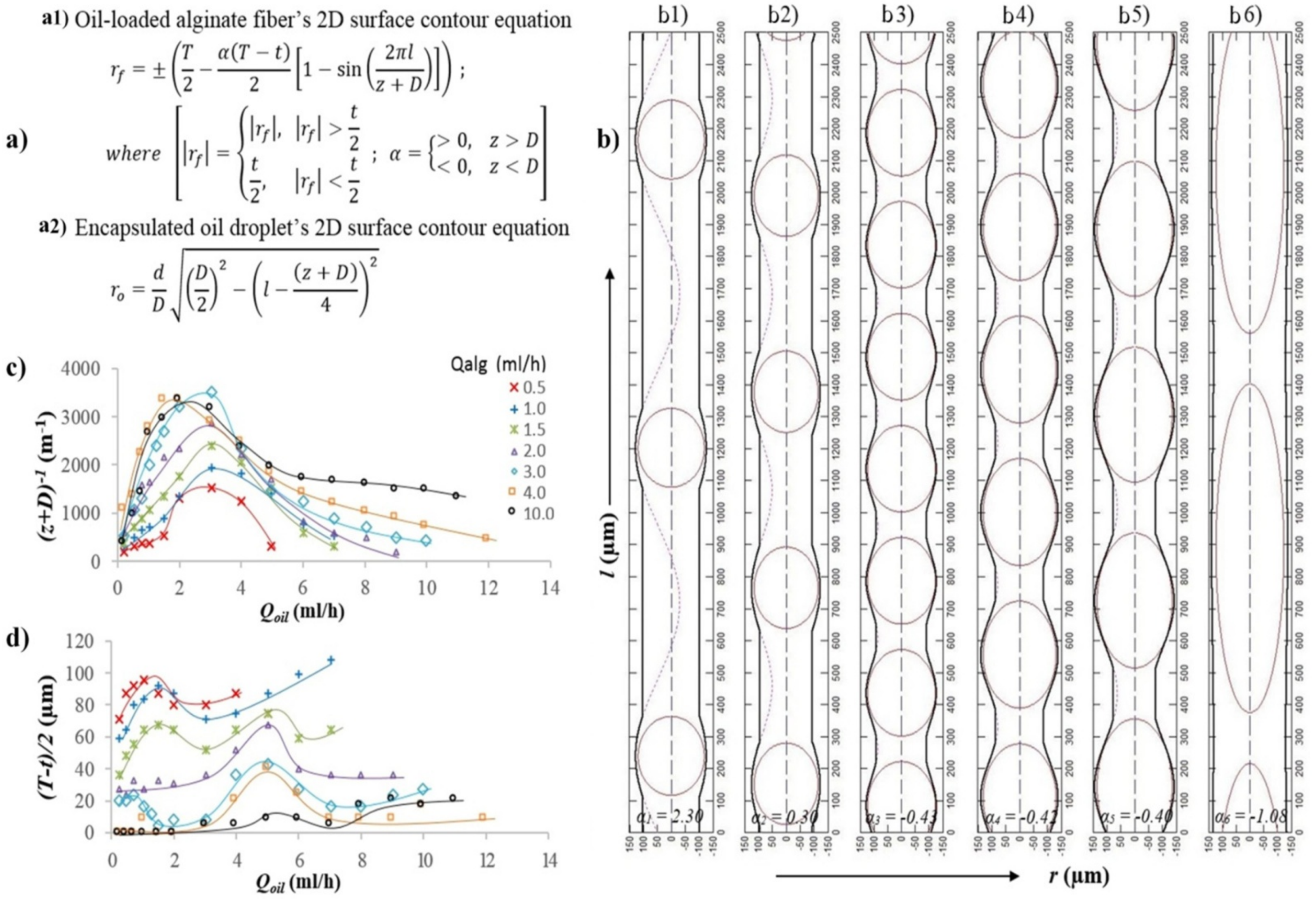

**Figure 3** **(a)** The sinusoidal function $r_f$ with the constraints (a1), and the elliptical function $r_o$ (a2) are presented, which were fitted to the 2-D surface profiles of the fibers and oil encapsulates, respectively. The common legends are shown in (a). **(b)** A two-dimensional mathematical reconstruction ($l$ versus $r$) of the surface contours of the fibers shown in Figure 1c ($Q_{oil}$= 0.5 ml/h - 6 ml/h), along with their oil encapsulates. Variations in the occurrence frequency of oil encapsulates per unit length along the fiber ($(z+D)^{-1}$), and corresponding changes in amplitudes ($(T-t)/2$) with $Q_{oil}$ are shown in **(c)** and **(d)**, respectively.

The frequency and amplitude of fibers can be used as appropriate measures for the *degree of waviness* of a fiber, as shown in Figure 3a1. Fibers with higher frequency and amplitude demonstrate a higher degree of waviness. Fibers with a higher degree of waviness are more useful for making nonwoven fabrics and pads, as they have better interlocking among themselves. Figure 3c shows the frequency of oil segments, in terms of per unit length, and Figure 3d shows the amplitude.

The frequency $[(z+D)^{-1}]$ increased with increasing $Q_{alg}$ because of the associated reduction in droplet (encapsulate) size with increasing drag. The highest frequency was observed at an intermediate $Q_{oil} \approx$ 3 ml/h for all sets, which is marked by the change in droplet geometry from spherical to prolate ellipsoids (Figure 3d3) and the associated increase in the axial length ($D$). The amplitude $[(T\text{-}t)/2]$ decreased with increasing $Q_{alg}$ (Figure 4d) because of the associated reduction in droplet size (due to increasing drag) and increase in $t$. The amplitude showed two peaks when $Q_{oil}$ was varied. The first peak, which occurred at a relatively low $Q_{oil}$ (≈ 1.5 ml/h) was more prominent at low $Q_{alg}$. The second peak was observed around $Q_{oil} \approx$ 5 ml/h beyond which the amplitude decreased as the fibers surface flattened because of the oil entities being transformed from prolate ellipsoidal into plug-like shapes (Figure 1c and 3d5).

These variations in frequency and amplitude with oil phase flow rate point to a criterion that the highest frequency occurs when the oil segments transform from spheres into prolate ellipsoids, while the maximum amplitude occurs at the transition between the ellipsoidal and plug-like shapes.

### *3.2.2 Spillage ratio*

Another feature of fibers related to, but not equivalent to, their wavy structure is *spillage ratio*, which measures the continuity of the encapsulated phase in a microfiber. It can be defined as the volume of each segment over total volume of the encapsulated oil per unit length or volume of the fiber and it signifies the relative mass loss of encapsulated materials due to accidental damage. The spillage ratio also indicates ease of splitting the fibers. The continuity of the oil medium in the tubular fibers also prevents their efficient splitting as the core material would escape out from the point of rupture, which can pose a significant practical hindrance in fiber handling.

A high frequency fiber has a small spillage ratio, but a fiber with large amplitude has a high spillage ratio. Fibers with the lowest frequency and amplitude, the straight fibers, have an extremely high spillage ratio when $D >> z$ but an extremely low spillage ratio when $z >> D$. The tubular encapsulation may provide a higher encapsulation ratio than any other configurations, as shown in Figure 1d, but it suffers from severe loss of encapsulated materials (high spillage ratio) in the case of accidental rupture of the alginate shell at any location along the fiber.

### *3.2.3 Tensile properties*

The tensile testing of the fibers was conducted with the help of a force-sensing device (DCA-100, First Ten Angstroms), a schematic of which is shown in Figure S1a (See Supporting Information). All the fibers were cut to a fixed length of 3 cm for mounting, with one end glued to the metal hanger on the top, while the other end glued to the bottom stage (Figure S1a1). To perform the uni-axial tensile testing, the bottom stage was moved down at a fixed velocity (0.2 mm/s) until the fiber broke off.

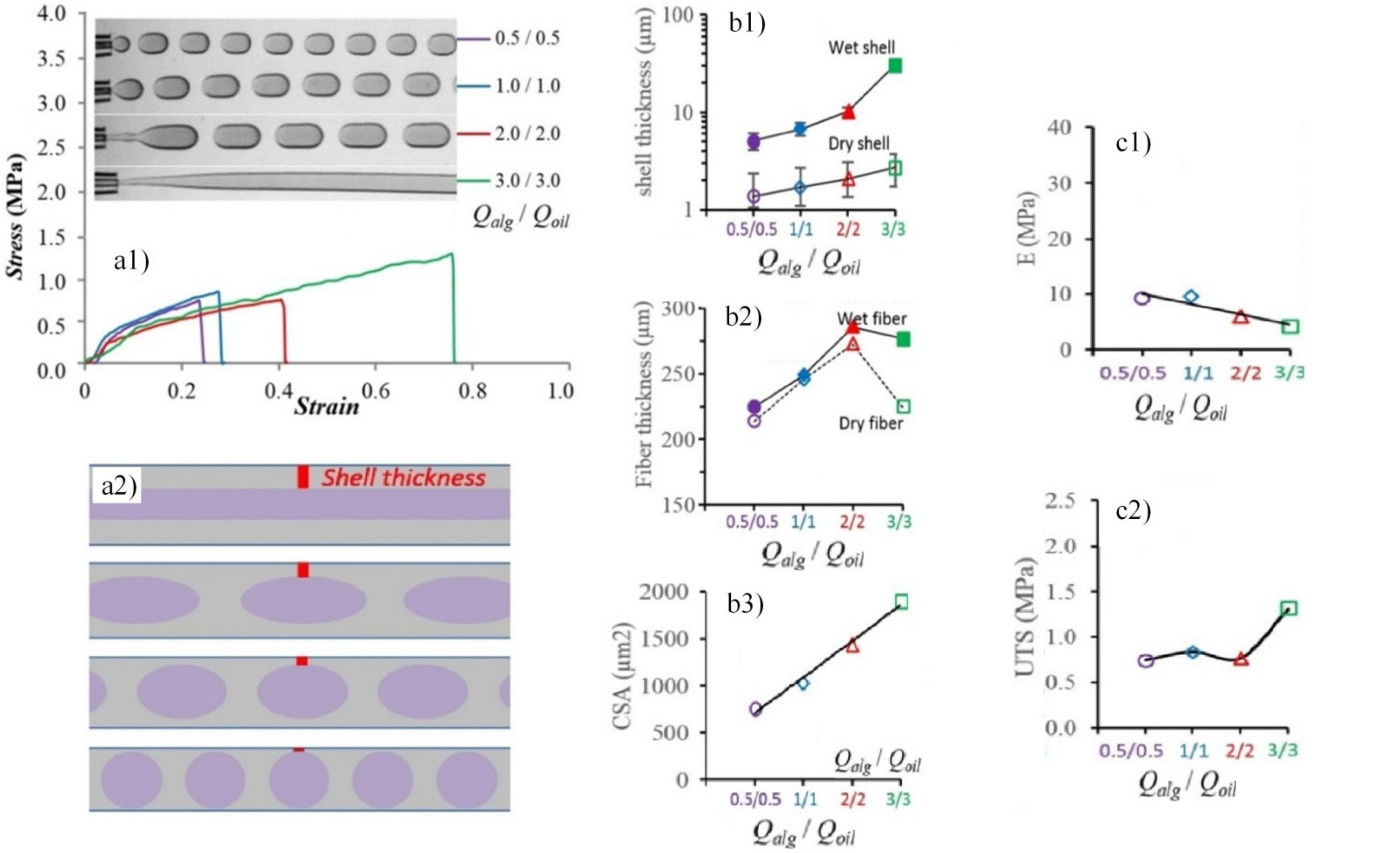

a) Shell thickness versus geometry b) Fiber dimensions c) Fiber tensile characteristics

**Figure 4** **(a)** The tensile testing results, obtained in terms of 'stress versus strain' for four dye-free fibers containing different encapsulate geometries at a fixed flow rate ratio $Q_{alg}/Q_{oil}$ are shown in (a1). The variation in minimum shell thickness for tubular, plug-like, ellipsoidal and spherical encapsulates are shown in (a2). **(b)** The variations in shell thickness, fiber thickness and the cross-sectional area (*CSA*) of corresponding fibers versus $Q_{alg}/Q_{oil}$ are shown in (b1)-(b3), respectively. **(c)** The calculated Young's modulus (*E*) and the measured ultimate tensile stress (*UTS*) versus $Q_{alg}/Q_{oil}$ are presented in (c1) and (c2), respectively. All figures represent $\phi_{alg}$ = 0.50.

The raw data was obtained in terms of the force experienced by the metal hanger attached to a fiber at a given strain. This data gave the maximum force ($F_{max}$) a fiber could withstand when axially pulled. The force-stress data were then processed to calculate the tensile stress on the fiber. A typical stress vs. strain curve, which defines the standard features associated with the tensile testing, is shown in Figure S1b.

The two main parameters characterizing fibers are the Young's Modulus (*E*) and the Ultimate Tensile Strength (*UTS*). The *E* is a measure of resistance of a fiber to any change within recoverable (*elastic*) deformation limits under tensile loading, while the *UTS* represents the maximum tensile stress a fiber can take before failure. To calculate the stress, the shell thickness of fibers at the thinnest points [$(T-d)/2$], as seen in Figure 1b, was measured and considered as the cross-sectional area (*CSA*) of dry or wet states. However, for tubular fibers the shell thickness, which was uniform across the fibers, was simply used as *CSA*. Since the tensile testing was performed on dehydrated fibers (Figure S1a2), which is the common state of fibers used for scaffold fabrication, the shell thickness in dried state was used for stress calculations.

To understand the impact of the encapsulated droplet morphology on the fibers mechanical properties, we compared four fibers with different encapsulate geometries at a fixed alginate phase ratio $\phi_{alg}$ = 0.50 corresponding to $Q_{alg}/Q_{oil}$ = 1 ($\phi_{alg} = Q_{alg} / (Q_{alg} + Q_{oil})$). Figure 4a1 shows the stress-strain curves of these fibers. Fibers with tubular configuration had the highest mechanical strength in terms of the failure load ($F_{max}$) and ultimate tensile strength (*UTS*) among all fibers (Figure S2 and Figure 4c2). This is because the tubular geometry provides the largest shell thickness (Figure 4b1) and shell cross-sectional area (Figure 4b3) at a fixed $\phi_{alg}$, as compared to other fibers having segmented oil encapsulates. Tubular fibers enjoy the thickest shell because they do not have pure alginate threads ($z$ = 0) as encountered in other morphologies. Also, the (minimum) shell thickness is quite small for discrete encapsulates, as the nodal spaces between adjacent droplets are filled by the alginate phase, which leaves less alginate volume around the oil segments in the fiber periphery.

Within discrete encapsulates, the minimum shell thickness decreased as the segment shape changed from tubular to plug, ellipsoidal and spherical (Figure 4a2). Fibers with tubular oil entity underwent the highest deformation (strain) before failure, and also had the smallest Young's Modulus (*E*) (Figure 4c1), which suggests that these fibers are easy to deform within their elastic limits.

We also studied the effect of varying $\phi_{alg}$ on the mechanical properties of the fibers for two extreme geometries, spherical and tubular (Figure 5). For both cases, when the $\phi_{alg}$ was increased by increasing $Q_{alg}$, the fiber with higher $\phi_{alg}$ showed improved mechanical strength in terms of the failure load ($F_{max}$) and ultimate tensile strength (*UTS*) (Figure 5a-5b, Figure S3).

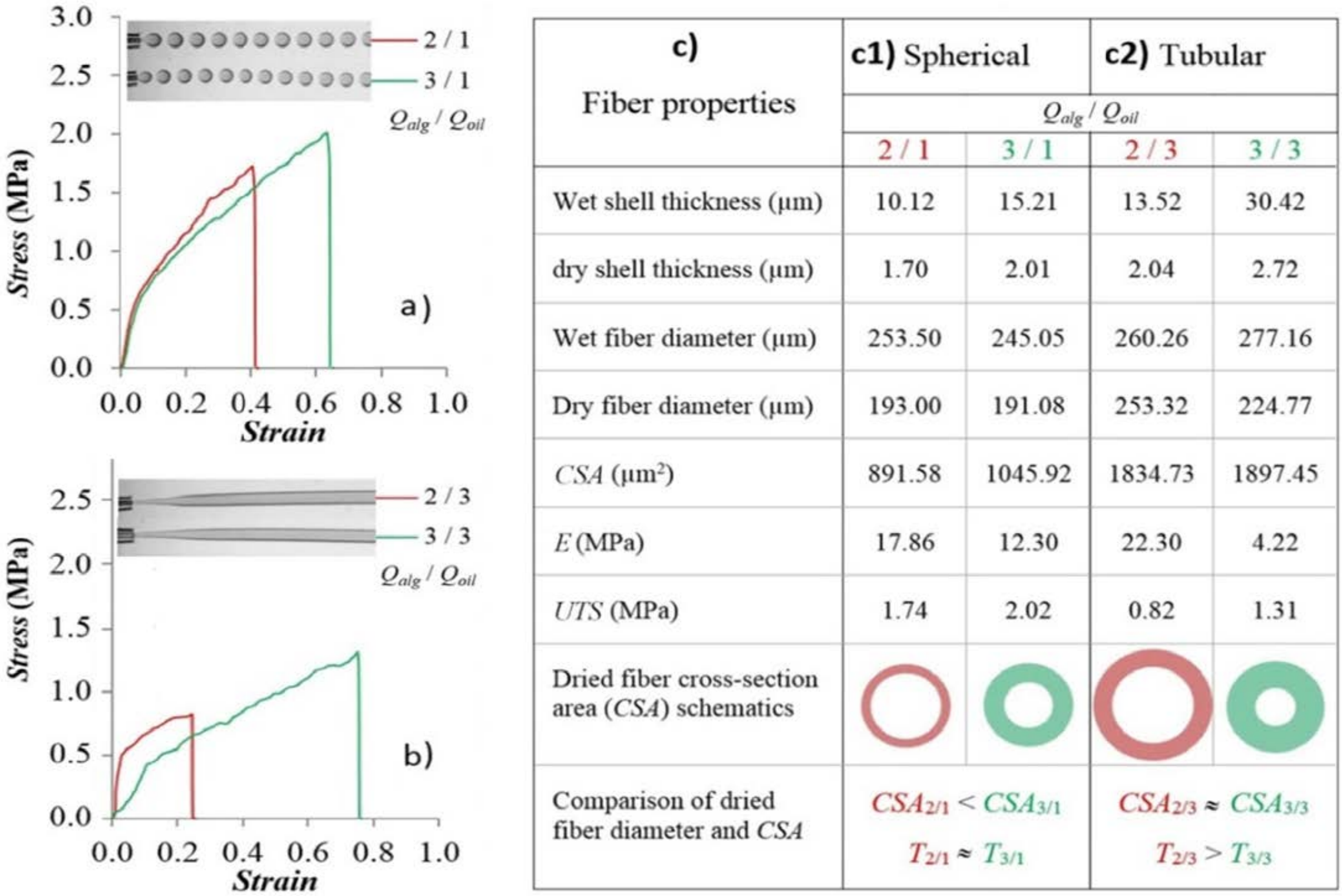

| **c)** Fiber properties | **c1)** Spherical | | **c2)** Tubular | |
|---|---|---|---|---|
| | $Q_{alg}$ / $Q_{oil}$ | | | |
| | 2 / 1 | 3 / 1 | 2 / 3 | 3 / 3 |
| Wet shell thickness (μm) | 10.12 | 15.21 | 13.52 | 30.42 |
| dry shell thickness (μm) | 1.70 | 2.01 | 2.04 | 2.72 |
| Wet fiber diameter (μm) | 253.50 | 245.05 | 260.26 | 277.16 |
| Dry fiber diameter (μm) | 193.00 | 191.08 | 253.32 | 224.77 |
| *CSA* (μm²) | 891.58 | 1045.92 | 1834.73 | 1897.45 |
| *E* (MPa) | 17.86 | 12.30 | 22.30 | 4.22 |
| *UTS* (MPa) | 1.74 | 2.02 | 0.82 | 1.31 |
| Dried fiber cross-section area (*CSA*) schematics | ○ | ○ | ○ | ○ |
| Comparison of dried fiber diameter and *CSA* | $CSA_{2/1} < CSA_{3/1}$<br>$T_{2/1} \approx T_{3/1}$ | | $CSA_{2/3} \approx CSA_{3/3}$<br>$T_{2/3} > T_{3/3}$ | |

**Figure 5** The Stress versus Strain data for fibers with **(a)** spherical and **(b)** tubular encapsulate geometry are compared at two different flow rate ratio $Q_{alg}/Q_{oil}$. **(c)** Fibers structural and tensile properties of spherical (c1) and tubular (c2) fibers used in (a) and (b), respectively. $Q_{alg}/Q_{oil}$. = 2/1 and 3/1 correspond to $\phi_{alg}$ = 0.67 and 0.75, respectively, while $Q_{alg}/Q_{oil}$. = 2/3 and 3/3 correspond to $\phi_{alg}$ = 0.40 and 0.50, respectively.

This is plausible as one can expect the minimum shell thickness and cross-sectional area of the fibers to increase with increasing $\phi_{alg}$, as observed for fibers with spherical oil droplets (Figure 5c1). The mechanical strength also improved with increasing $\phi_{alg}$ in the case of tubular fibers; however, this was achieved despite the two tubular fibers having a similar cross-sectional area (Figure 5c2). This occurred because the increase in $\phi_{alg}$ resulted in the formation of a thinner fiber but with a thicker shell. We can conclude that for tubular fibers with similar *CSA* but different dimensions, the fiber with smaller diameter is stronger because of having a thicker shell. We also found that the fiber with higher $\phi_{alg}$ showed a poorer resistance to elastic deformation (low *E*), and also underwent more plastic deformation.

We now analyse the impact of simultaneous variations in $\phi_{alg}$ and encapsulate geometry on the fiber properties (Figure 6). To bring about such variations, $\phi_{alg}$ was increased by decreasing $Q_{oil}$ in such a way that the tubular oil-encapsulate disintegrated into discrete entities due to the associated increase in drag (Figure 6a). In this case, the tubular and spherical configuration had the lowest and highest

$\phi_{alg}$, respectively. However, the tubular fiber was still able to withstand almost the largest tensile load ($F_{max}$) (Figure S4), in spite of having the minimum $\phi_{alg}$. This is because the tubular fiber still had the largest cross-sectional area among all fiber types, due to the geometrical advantage in terms of shell thickness (Figure 6a2). However, its large *CSA* minimized the *UTS* considerably (Figure 6b3 and 6c2).

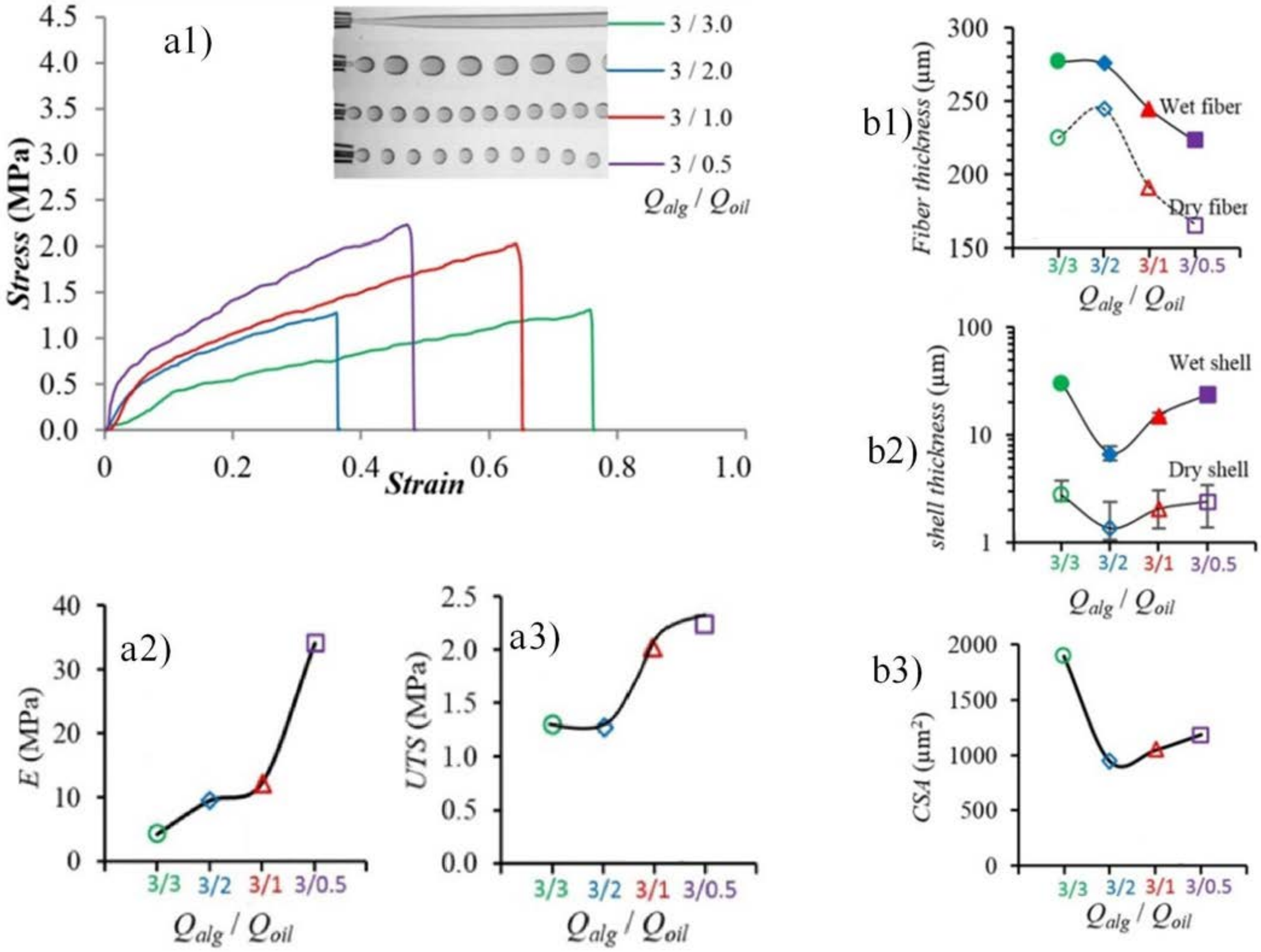

**Figure 6** **(a)** The variations in stress against the measured strain for fibers with varying geometry and $\phi_{alg}$ are compared in (a1). The variations in fibers tensile properties *E* and *UTS* against $Q_{alg}/Q_{oil}$ are presented in (a2) and (a3) respectively. **(b)** The variation in fiber thickness, shell thickness and cross-sectional area (CSA) against $Q_{alg}/Q_{oil}$ are shown in (b1), (b2), and (b3) respectively. $Q_{alg}/Q_{oil}$ = 3/3, 3/2, 3/1, and 3/0.5 correspond to $\phi_{alg}$ = 0.50, 0.60, 0.75, and 0.85, respectively.

Tubular fibers, which had the lowest $\phi_{alg}$, underwent maximum plastic and elastic deformation, as indicated by a minimum *E* (Figure 6c1). This was a net result of two opposing effects on *E*, one arising from the tubular geometry and the other from the low $\phi_{alg}$. As observed earlier, the tubular geometry showed the smallest *E* among all geometries at a given $\phi_{alg}$ (Figure 4c1). For all geometries, $E$ increased with deceasing $\phi_{alg}$ (Figure 5). Thus, a large deformation of the tubular fiber at low $\phi_{alg}$ indicates that the impact of encapsulate geometry outweighed the effect of $\phi_{alg}$ on $E$, which highlights the significance of encapsulate morphology on the mechanical properties of fibers.

It has been shown in the literature that mechanical properties of alginate microfibers are consistently improved with increasing alginate and calcium concentrations. However, for the latter there is a critical concentration above which the strength of fibers is reduced.[28] This strengthening effect is not surprising as these two reactants form the backbone of crosslinked alginate microfibers. We therefore expect alterations in these variable below the critical concentration would not alter the strength order of fibers as well as the conclusion made in this work. Furthermore, we anticipate the impact of size on comparative properties of fibers remain similar when the fiber dimensions are linearly scaled (up or down) provided that the fiber composition and encapsulate geometry are preserved. However, the introduction of the unified single-step encapsulation method for fabrication of a wide range of morphologies opens up opportunities for further in-depth investigation of the impact of variables including alginate and $CaCl_2$ concentrations, rehydration, and fibers diameter and bundling on the mechanical properties of compound alginate microfibers.

## 4. Conclusions

A facile one-step microfluidic encapsulation approach was employed to conveniently tune the geometry of oil-encapsulates in alginate microfibers. The technique was based on the simultaneous formation and encapsulation of the oil phase. Using this method, one is able to tune the encapsulate shape across a wide spectrum of geometries (spherical, ellipsoidal, plug-like and tubular) at a fixed fiber composition (e.g., constant alginate phase ratio $\phi_{alg}$). Additionally, the shape of the oil encapsulates could also be altered by making a more resilient (deformation-resistant) calcium alginate shell via using high alginate and calcium chloride concentrations. This provides an opportunity to produce a comprehensive set of data for a wide range of fibers formed under the same conditions, which facilitates comparative study of physical and mechanical features of the fibers. The methodology can assist the selection of fibers for any particular application based on desired properties.

To assess the degree of waviness, a 2D mathematical reconstruction of fibers surface profile was presented. In this reconstruction, a sinusoidal wave was fitted to the surface morphology of fibers. A high frequency and a high amplitude for the wave function correspond to a high degree of waviness. The maximum frequency was noted in the fibers closely packed with spherical encapsulates, while the maximum amplitude was observed in the fibers fully packed with ellipsoidal encapsulates. Fibers with spherical encapsulates were limited to a low encapsulation volume, but enjoyed a low spillage ratio. On the other hand, fibers with tubular encapsulates had the highest encapsulation volume, but also suffered from the highest spillage ratio, meaning they were prone to a colossal core-loss in case of an accidental fracture of the fiber.

In terms of tensile properties, tubular fibers were able to endure the maximum tensile force ($F_{max}$) before failure at given alginate phase ratio $\phi_{alg}$, compared to fibers with other encapsulate geometries. Fibers with a given encapsulate geometry withstood a higher tensile force at higher $\phi_{alg}$. However, the strength of fibers is reduced if the increase in $\phi_{alg}$ is associated with alteration in the encapsulate geometry from tubular to discrete oil segments. Regarding fiber deformation, tubular fibers underwent maximum elastic and plastic deformation prior to failure.

## Acknowledgements

We acknowledge the use made of Photron FastCam SA-5 (monochrome) high-speed video recording system, which was borrowed from the EPSRC (Engineering and Physical Sciences and Research Council) Engineering Instrument Pool.

## References

---

[1] R. Mahsood and M. Miraftab, *J. Wound Care,* 2014, **23**, 3, 153-159.

[2] J. Sun and H. Tan, *Materials,* 2013, **6**, 4, 1285-1309.

[3] S.Y. Ahn, C.H. Mun and S.H. Lee, *RSC Adv.,* 2015, **5**, 20, 15172-15181.

[4] H. Onoe and S. Takeuchi, *Drug Discov. Today,* 2015, **20**, 2, 236-246.

[5] M.A. Daniele, D.A. Boyd, A.A. Adams and F.S. Ligler, *Adv. Healthcare Mater.,* 2015, **4**, 1.

[6] Y. Luo, A. Lode and M. Gelinsky, *Adv. Healthcare Mater.,* 2013, **2**, 6, 777-783.

[7] J.F. Mano, G.A. Silva, H.S. Azevedo, P.B. Malafaya, R.A. Sousa, S.S. Silva, L.F. Boesel, J.M. Oliveira, T.C. Santos, A.P. Marques, N.M. Neves and R.L. Reis, *J. R. Soc. Interface,* 2007, **4**, 17, 999-1030.

[8] Z. Izadifar, X. Chen and W. Kulyk, *J. Funct. Biomater.,* 2012, **3**, 4, 799-838.

[9] C. Colosi, M. Costantini, R. Latini, S. Ciccarelli, A. Stampella, A. Barbetta, M. Massimi, L.C. Devirgiliis and M. Dentini, *J. Mater. Chem. B,* 2014, **2**, 39, 6779-6791.

[10] S. Hong , D. Sycks , H.F. Chan , S. Lin , G.P. Lopez , F. Guilak , K.W. Leong , and X. Zhao, *Adv. Mater.*, 2015, **27**, 4035–4040

[11] P. Calvert, *Adv. Mater.*, 2009, **21**, 743–756

[12] A.S. Chaurasia, F. Jahanzad and S. Sajjadi, *Chem. Eng. J.* 2017, **308**, 1090-1097.

[13] Y. Cheng, F. Zheng, J. Lu, L. Shang, Z. Xie, Y. Zhao, Y. Chen and Z. Gu, *Adv. Mater.* 2014, ***26***, 5184.

[14] Y. Yu, H. Wen, J. Ma, S. Lykkemark, H. Xu and J. Qin, *Adv. Mater.,* 2014, **26**, 16, 2494-2499.

[15] X. He, W. Wang, K. Deng, R. Xie, X. Ju, Z. Liu and L. Chu, *RSC Adv.,* 2015, **5**, 2, 928-936.

[16] T. Sun, C. Hu, M. Nakajima, M. Takeuchi, M. Seki, T. Yue, Q. Shi, T. Fukuda and Q. Huang, *Microfluid. Nanofluid.,* 2015, +**18**, 5-6, 1177-1187.

[17] E. Um, J.K. Nunes, T. Pico and H.A. Stone, *J. Mater. Chem. B,* 2014, **2**, 45, 7866-7871.

[18] A.S. Chaurasia and S. Sajjadi, *Small,* 2016, **12**, 30, 4146.

[19] X. He, W. Wang, Y. Liu, M. Jiang, F. Wu, K. Deng, Z. Liu, X. Ju, R. Xie and L. Chu, ACS Appl. Mater. Interfaces, 2015, 7, 31, 17471-17481.

[20] K.A. Kwon, R. J. Shipley, M. Edirisinghe, D. G. Ezra, G. E. Rose, A. W. Rayment, S. M. Best and R. E. Cameron, *Mater. Sci. Eng. C*, 2014, **35**, 220–230.

[21] A. Mirabedini, J. Foroughi, T. Romeo and G.G. Wallace, *Macromol. Mater. Eng.,* 2015, **300**, 12, 1217-1225.

[22] K. Dey, R.A. Khan, A.M.S. Chowdhury, *Polym. Plast. Technol. Eng.,* 2011, **50**, 7, 698-704.

[23] L. Liu, L. Jiang, G.K. Xu, C. Ma, X.G. Yang and J.M. Yao, *J. Mater. Chem. B,* 2014, **2**, 43, 7596-7604.

[24] Y. Cheng, Y. Yu, F. Fu, J. Wang, L. Shang, Z. Gu and Y. Zhao, *ACS Appl. Mater. Inter.* 2016, ***8***, 1080.

[25] A.S. Chaurasia and S. Sajjadi, *Chem. Eng. Sci.,* 2015, **129**, 260-270.

[26] A.S. Chaurasia, D.N. Josephides and S. Sajjadi, *Chemphyschem,* 2015, **16**, 2, 403-411.

[27] Y. Jun, E. Kang, S. Chae and S.-H. Lee, *Lab Chip,* 2014, **14**, 2145.

---

[28] T. R. Cuadros, O. Skurtys, J. M. Aguileraa, *Carbohydrate Polymers*, 2012, **89**, 1198–1206